

Room-Temperature Exciton-Polariton-Driven Self-Phase Modulation in Planar Perovskite Waveguides

Nikita V. Glebov, Mikhail A. Masharin, Alexei Yulin, Alexey Mikhin, Md Rumon Miah, Hilmi Volkan Demir, Dmitry N. Krizhanovskii, Vasily Kravtsov, Anton K. Samusev,* and Sergey V. Makarov*



Cite This: *ACS Nano* 2025, 19, 14097–14106



Read Online

ACCESS |



Metrics & More



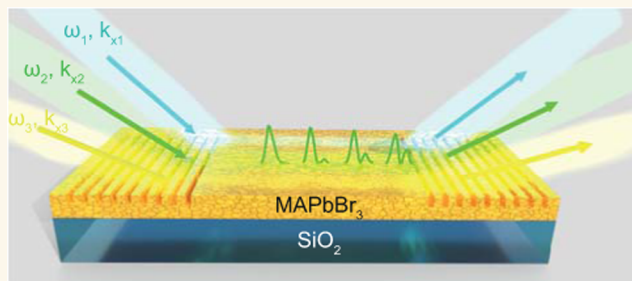
Article Recommendations



Supporting Information

ABSTRACT: Optical nonlinearities are crucial for advanced photonic technologies since they allow photons to be managed by photons. Exciton-polaritons resulting from strong light–matter coupling are hybrid in nature: they combine the small mass and high coherence of photons with strong nonlinearity enabled by excitons, making them ideal for ultrafast all-optical manipulations. Among the most prospective polaritonic materials are halide perovskites since they require neither cryogenic temperatures nor expensive fabrication techniques. Here, we study strikingly nonlinear self-action of ultrashort polaritonic pulses propagating in planar MAPbBr₃ perovskite slab waveguides. Tuning the input pulse energy and central frequency, we experimentally observe various scenarios of its nonlinear evolution in the spectral domain, which include peak shifts, narrowing, or splitting driven by self-phase modulation, group velocity dispersion, and self-steepening. The theoretical model provides complementary temporal traces of pulse propagation and reveals the transition from the birth of a doublet of optical solitons to the formation of a shock wave, both supported by the system. Our results presented here represent an important step in ultrafast nonlinear on-chip polaritonics in perovskite-based systems.

KEYWORDS: halide perovskite, nanoimprint lithography, nonlinear optical waveguide, exciton-polariton, self-phase modulation, group velocity dispersion, soliton



One of the most important tasks of modern nanophotonics is leveraging nonlinear optical effects for efficient light manipulation at the nanoscale, enabling the development of ultrafast, compact photonic devices and circuitry. Particular applications of nonlinear nanophotonics include ultrafast signal processing and full optical switches,^{1,2} supercontinuum light generation,^{3,4} or ultrashort pulse generation.⁵ Nonlinear effects arise from photon–photon interactions that are mediated by materials. These effects are naturally weak because they depend on the nonlinear response of the material to electromagnetic fields.⁶ However, they can be significantly strengthened in environments where the electromagnetic field and photon–photon interaction are enhanced by specific material mechanisms, such as the formation of exciton-polaritons in semiconducting structures.⁷

Exciton-polaritons are bosonic quasi-particles formed through the strong coupling of light and matter, garnering significant attention due to their unique properties.⁸ The

photonic component of exciton-polaritons offers high group velocity,⁹ low effective mass, and extended coherence times,^{10,11} while the excitonic component introduces strong nonlinearity driven by Coulomb interactions between the quasi-particles, which can significantly enhance the corresponding nonlinear optical response.^{12–14} The Kerr nonlinearity in such systems can be 3–4 orders of magnitude stronger than in typical semiconductor or dielectric materials, where light couples only weakly to crystal excitations.¹⁵

One of the most extensively studied and commonly utilized material platforms for exciton-polariton systems is the GaAs-

Received: December 27, 2024

Revised: March 18, 2025

Accepted: March 19, 2025

Published: April 1, 2025



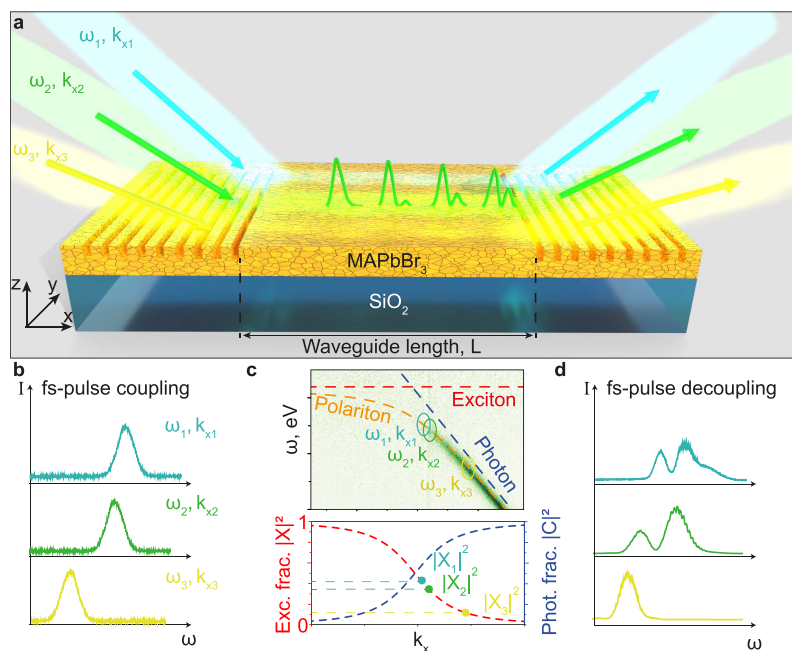


Figure 1. Propagation of exciton-polariton wavepackets in a halide perovskite waveguide. (a) Sketch of the studied system, demonstrating the processes of coupling/decoupling of light into/from the waveguide for three different detunings. The spectrum of the propagating pulse undergoes self-phase modulation and nonlinear group velocity dispersion, as illustrated schematically on the waveguide surface. (b) Spectra of femtosecond pulses incident on the coupler for three different detunings. (c) Top: Measured angle-resolved transmittance spectrum from the decoupler with excitation by white light. The red and dark blue dashed lines correspond to uncoupled exciton and photon. The orange dashed line represents polariton. Ellipses show polariton states with particular energies and wavevectors excited resonantly using a femtosecond laser. Bottom: Calculated Hopfield coefficients as a function of the wavenumber. (d) Spectra of femtosecond pulses transmitted through the in-plane wavevector for three different detunings.

based quantum well (QW).^{11,16,17} Despite the huge progress in this field recently, this platform has low exciton binding energy, which limits it to cryogenic temperatures.^{18,19} This temperature constraint can be addressed using wide-bandgap semiconductor QWs like ZnO²⁰ or GaN,²¹ although usually, these materials require complex and costly fabrication techniques, such as epitaxial growth. Recently, monolayer transition metal dichalcogenides have emerged as promising candidates for room-temperature polariton systems,²² yet their practical applications remain limited by challenges in scalable manufacturing.

Planar systems such as metasurfaces and waveguides are among the most promising platforms for on-chip communication and data processing nowadays. However, the nonlinear response of polaritonic guided systems at room temperature remains largely unexplored, even though these systems have the potential to exhibit various nonlinear phenomena, including solitons¹⁸ and pulse modulation.^{23,24} Halide perovskites exhibit remarkable excitonic properties, making room-temperature applications much more feasible, and offer the advantage of easy and cost-efficient fabrication.^{25–27} Perovskites have recently shown their potential for advanced applications, as demonstrated by successful room-temperature vertical cavity surface emitting lasers,^{28,29} optical switching,³⁰ and edge lasing from a crystalline waveguide.³¹ However, the vertical geometry poses challenges for integration into compact, planar photonic circuits on a chip due to its inherently larger vertical dimensions.

In this work, we study the nonlinear propagation of guided exciton-polariton pulses in a planar perovskite-based waveguiding system at room temperature. We inject (extract) femtosecond pulses into (from) the waveguide using resonant

grating couplers imprinted in the perovskite waveguide. As the fluence of the input pulse increases, the spectral shape of the pulse transforms during its propagation through the waveguide due to the interplay of self-phase modulation (SPM), group velocity dispersion (GVD), waveguide dispersion, the influence of the exciton reservoir, and other processes. Self-phase modulation is a nonlinear optical effect where a pulse's phase shifts due to intensity-dependent changes in the medium's refractive index, broadening the pulse spectrum. Microscopically, this effect arises from polariton-polariton scattering, where polariton pairs interact and redistribute energy across different frequencies, effectively modulating the pulse phase as it propagates. The experimental results are supported by numerical simulations of the studied system. Numerical analysis further reveals that SPM induces the temporal splitting of the input pulse into two separate pulses, influenced by strong spectrally inhomogeneous dispersion and nonlinearity inherent to the polaritonic nature of the system. Our experimental findings, showing wavelength- and distance-dependent femtosecond pulse evolution, align well with the theoretical model, allowing us to explicitly interpret the observed phenomena. Our results demonstrate how tuning the pump energy in the guided polaritonic system enables the transition between different nonlinear regimes, such as shock waves and solitons, with potential applications in all-optical chips.

EXPERIMENT

In our experiments, we fabricate planar waveguides based on MAPbBr₃ thin films (see the schematic illustration in Figure 1a). One of the key advantages of halide perovskites

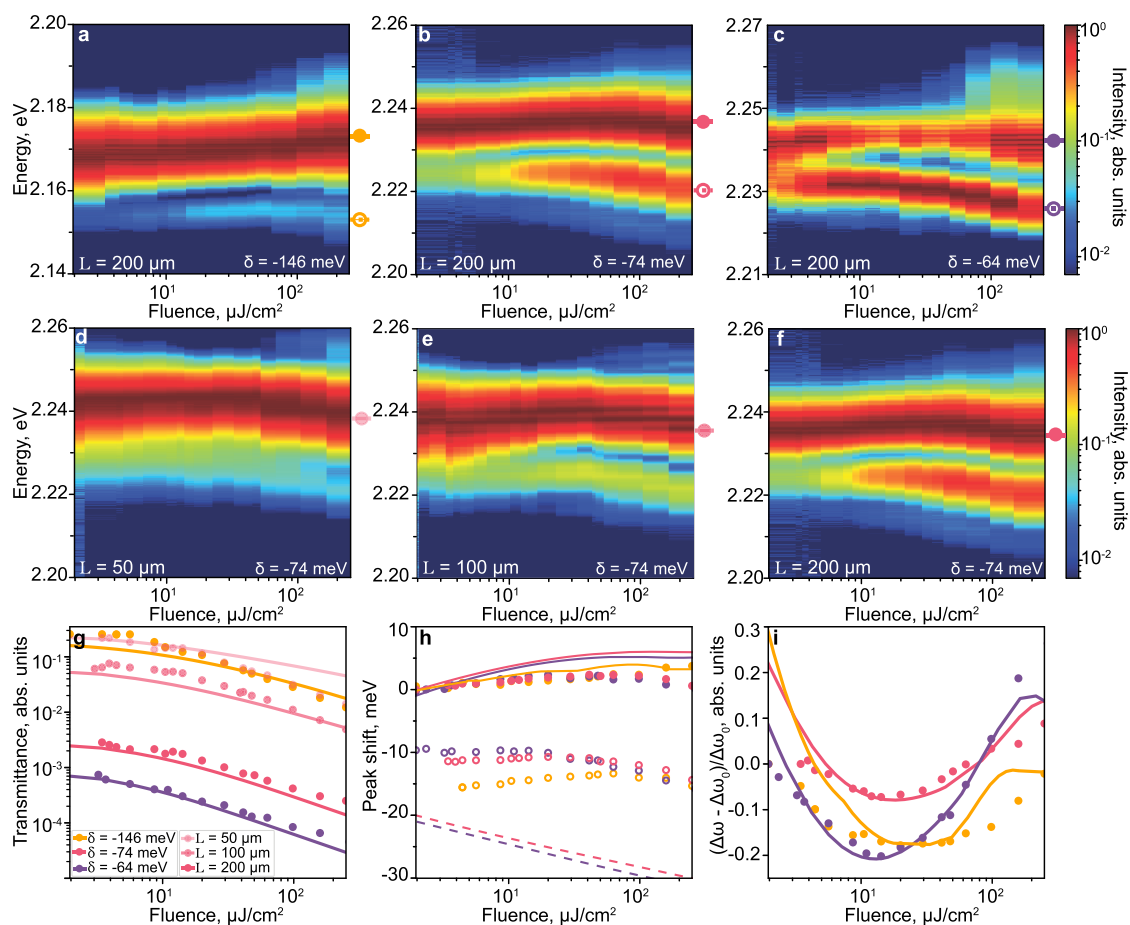


Figure 2. Experimental results on laser pulse propagation in a perovskite planar waveguide in different spectral ranges. Normalized transmitted pulse spectra vs input fluence for (a–c) three different detunings from the exciton level and waveguide length $L = 200 \mu\text{m}$ and (d–f) three different waveguide lengths with the detuning $\delta = -74 \text{ meV}$. (g) Transmittance of the waveguide normalized on the pump fluence adjusted for the effectiveness of the coupler for different detunings and waveguide lengths. (h) Peak shift from the initial position at small fluence for two peaks (high-energy peak, filled circles; low energy peak, empty circles). (i) Relative spectral width of the output pulse normalized on the initial spectral width at the lowest fluence for different detunings. The lines correspond to theoretical calculations.

is that they can be synthesized through solution-based methods, enabling low-cost fabrication and making them highly promising for practical applications.³² Due to the relatively high refractive index of 2.1–2.3 in the 500–600 nm wavelength range,³³ a perovskite thin film works as a planar waveguide with subwavelength thickness. Due to its sublight-line dispersion, a waveguide mode cannot be excited directly in free space and requires a coupling mechanism to match the necessary wavevector.³⁴ One of the most effective and straightforward methods to excite waveguide modes is through the use of periodic structures such as grating couplers.³⁵ Various techniques can create periodic structures on halide perovskite surfaces, including nanoimprint lithography,^{36,37} mechanical scanning probe lithography,³⁸ and direct laser writing.³⁹ We chose nanoimprint lithography for its high resolution, direct pattern transfer, and compatibility with the soft crystal lattice of halide perovskites, making it particularly well suited for structuring these materials.

We employ the solution-based method via spin coating and nanoimprinting to fabricate planar waveguides with elements for coupling to the waveguide mode (see the [Methods](#) section). Glass molds are prepared by electron beam lithography, following established protocols (see the [Methods](#) section). The final system comprises three key elements: a

grating coupler, an unstructured planar waveguide, and an identical grating decoupler. Several samples with different waveguide lengths have been fabricated and studied, with distances between couplers and decouplers ranging from 50 to 200 μm . The thickness of the waveguide is 110 nm, defined by the thickness of the MAPbBr₃ thin film. The gratings have a period of 280 nm, a modulation depth of 65 nm, and a fill factor of 0.48. The topography of the fabricated waveguide sample, as measured by atomic force microscopy (AFM), is shown in Supporting Information ([Figure S2a,c](#)). All geometrical parameters are selected based on numerical simulations to achieve waveguide modes near the exciton resonance of our material ($\sim 2.32 \text{ eV}$).

We perform measurements using a custom back-focal plane setup for angle-resolved transmission and reflection spectroscopy paired with a wavelength-tunable femtosecond laser and a halogen lamp for the excitation as schematically illustrated in [Figure S3a,b](#) (see the [Methods](#) section for details). In order to estimate the exciton-photon coupling strength in the perovskite waveguide, we first obtained the angle-resolved reflectance spectra by measuring the leaky modes of couplers. The experimental results ([Figure S4a](#)) show the dispersion of the waveguide leaky modes in the reflection. Dispersion of the waveguide leaky modes behavior demonstrates a strong

curvature near the exciton resonance, which is typical anticrossing behavior in strong-coupled systems.¹⁰

We fit the measured leaky modes with the two-coupled oscillators model^{10,40} (see the [Supporting Information](#) for details). The Rabi splitting and coupling constant are estimated with this model as $\Omega_R = 104$ and $g = 54$ meV, respectively. The estimated Rabi splitting and coupling constant satisfy the criteria of the light–matter strong coupling at room temperature as $\Omega_R > (\gamma_{\text{ex}} + \gamma_{\text{ph}})/2$ and $g > |\gamma_{\text{ex}} - \gamma_{\text{ph}}|/2$,^{41,42} since the estimated losses of uncoupled photons and excitons are $\gamma_{\text{ph}} = 16$ meV and $\gamma_{\text{ex}} = 14$ meV, respectively.

Transmission through the waveguide is measured by coupling incident TE-polarized white light (with the electric field parallel to the coupler grooves) into the input coupler and collecting the entire output signal from the decoupler (as shown in the inset of [Figure S3b](#) for a waveguide length of 50 μm). As a result, we obtained the angle-resolved linear transmittance spectrum of the waveguide mode ([Figure S4b](#)). We can observe only one branch of the dispersion with group velocity directed toward the decoupler, where the signal is collected. The spectral region of the dispersion close to the exciton level has low transmission due to excitonic absorption.

The nonlinear response of the exciton-polariton waveguide system is studied by utilizing the wavelength-tunable femtosecond laser pulses. Transmission of the laser pulses is measured using the same method mentioned above for the white light ([Figure 1a](#)). The incident angle and wavelength of the excitation laser are adjusted to achieve resonant pumping ([Figure 1b,c](#)), as detailed in the [Methods](#) section. We study the waveguide transmission as a function of the input fluence from resonant femtosecond pumping at various wavelengths (L) and detunings (δ) from the exciton resonance energy. Studied polariton states are demonstrated on the waveguide polariton dispersion by ellipses on the transmittance angle-resolved spectrum ([Figure 1c](#)). We consider three different detunings from the exciton resonance of -64 , -74 , and -146 meV, which correspond to Hopfield coefficients of excitonic fractions^{25,40} of $|X_1|^2 = 0.47$, $|X_2|^2 = 0.41$, and $|X_3|^2 = 0.15$ calculated as outlined in the [Supporting Information](#). Laser pulse transmittance spectra corresponding to the mentioned detunings are shown in [Figure 1d](#).

In the experiment, we measure the transmittance spectra of the fs-laser pulse across various detunings and waveguide lengths, presenting the normalized intensity spectra as a function of input fluence in [Figure 2a–c](#) for different detunings and in [Figure 2d–f](#) for different waveguide lengths. We generally observe spectral broadening of the output pulses with increasing pump fluence and the emergence of an additional peak. This effect is consistently observed across all energy detunings ([Figure 2a–c](#)) and waveguide lengths ([Figure 2d–f](#)). We observe the occurrence of an additional peak with a lower energy than the energy of the input pulse, the mechanism of which is explained in the [Discussion](#) section.

At a fixed waveguide length of 200 μm , the increasing of the excitation detuning leads to the attenuation of the second peak formation in the output pulse spectra ([Figure 2a–c](#)). At smaller detuning, the signal is narrower in general due to stronger absorption of the blue part of the pulse and more efficient propagation of the red part, both caused by the higher exciton fraction and increased nonradiative losses, whereas at larger detuning, reduced absorption results in a broader signal. At the maximal detuning of -146 meV, the low-energy peak emerges at the input fluence of approximately $10 \mu\text{J}/\text{cm}^2$, with

a notably smaller amplitude compared to that of the main peak ([Figure 2a](#)). At the minimal detuning of -64 meV, the low-energy peak occurs with a significant amplitude at the input fluence of approximately $4 \mu\text{J}/\text{cm}^2$ ([Figure 2c](#)). The formation of the low-energy peak is attributed to the nonlinear phase, which increases with a higher exciton fraction. Hence, at smaller detuning, the amplitude of the low-energy peak is more pronounced. Further details are provided in the [Discussion](#) section.

At a fixed detuning of -74 meV, the increasing propagation length causes the formation of a second peak in the spectra of the output pulse ([Figure 2d–f](#)). The generation of new frequency components occurs continuously along the propagation in the waveguide. The amplitude of the low-energy peak for a wavelength of 50 μm ([Figure 2d](#)) is so small within this fluence range that it is nearly indistinguishable from the main peak. However, in the longer waveguide of 200 μm , the low-energy peak becomes significantly more pronounced ([Figure 2f](#)). Additionally, as the waveguide length increases, the splitting between the low- and high-energy peaks begins to occur at progressively lower fluences. This behavior is due to the nonlinear phase shift, which is responsible for the formation of the low-energy peak, which increases with the propagation length of the pulse.

In order to describe the evolution of the pulses in the waveguide with the increase of incident fluence, we estimate the central frequency, line width, and amplitude of each peak (see the [Supporting Information](#) for details). [Figure 2h](#) (circles) shows the pump-fluence-dependent shift of the peak position. In the case of the largest detuning of -146 meV used in the experiment, the high-energy peak exhibits only a blue shift, while the low-energy peak shows both a blue shift and a subsequent red shift. At the other two detunings, -74 and -64 meV, the high-energy peak exhibits a blue shift followed by a red shift, while the low-energy peak shows a red shift. [Figure 2i](#) (circles) demonstrates the relative change in spectral line width with fluence, normalized to the low-fluence value. The spectral line width initially narrows and then broadens with fluence across all detunings and waveguide lengths.

THEORY

To gain an insight into the mechanisms governing the experimentally observed evolution of the propagating through the waveguide laser pulses with increasing incident fluence, we build upon the previously developed theoretical mode.²³ It incorporates the strong coupling between excitons and photons, exciton–exciton repulsion,²⁵ and interaction of quasi-particles with an incoherent exciton reservoir,⁴³ yielding the following system of equations:^{23,44–48}

$$\begin{cases} \partial_t A + v_g \partial_x A = -\gamma_{\text{ph}} A + i\Omega_R \psi + f_p(x, t), \\ \partial_t \psi = -(\gamma_{\text{ex}} + \gamma_{\text{res}}) \psi + i\Delta \psi - \Gamma \psi + i\Omega_R A, \\ \partial_t \rho = -\gamma_{\text{p}} \rho + 2\gamma_{\text{res}} |\psi|^2 \end{cases} \quad (1)$$

The first equation is written for the slowly varying amplitude A of the photon-guided mode. We approximate photonic dispersion in the studied range of wavevectors by a linear function with group velocity v_g evaluated at the exciton resonance frequency and dissipation rate γ_{ph} . The photonic component is excited by the driving force (currents) f_p

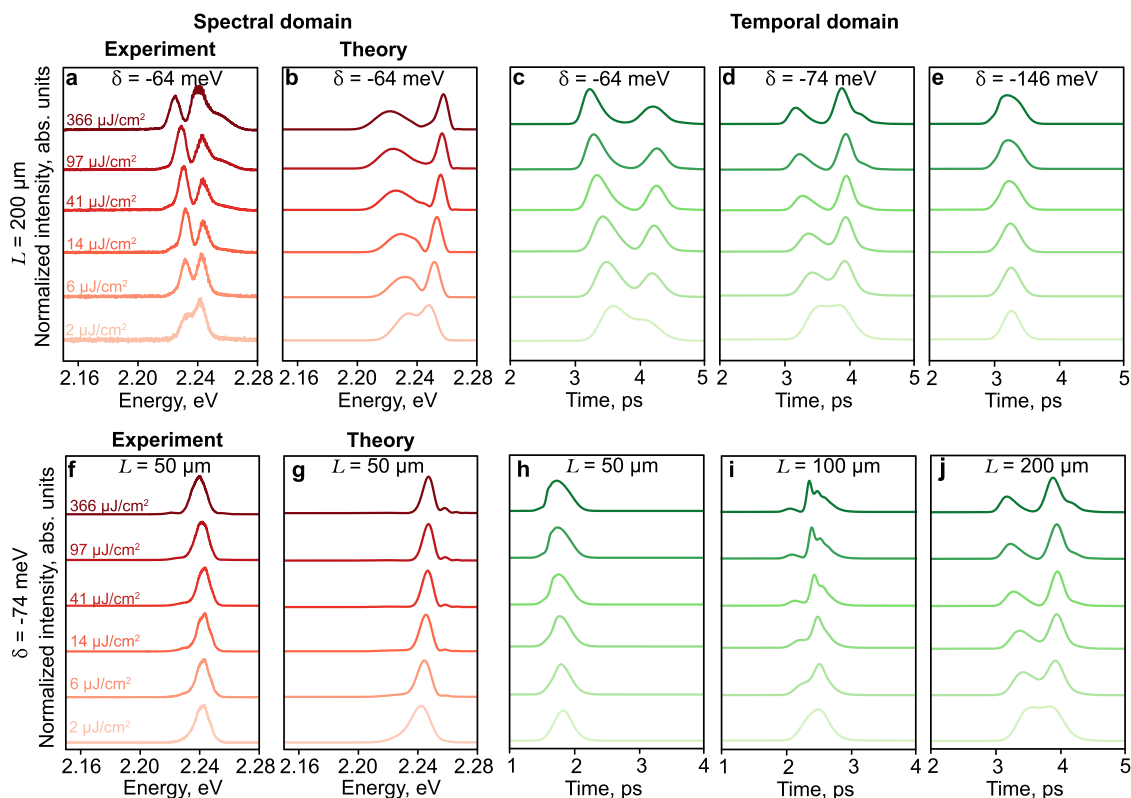


Figure 3. Theoretical modeling of laser pulse propagation in a planar perovskite waveguide. Normalized transmittance spectra plotted in the dependence of input fluence for the detuning of -64 meV and waveguide length of $200 \mu\text{m}$ and for the detuning of -74 meV and waveguide length of $50 \mu\text{m}$ (a, f) for the experiment and (b, g) theoretical calculation, respectively. Simulated normalized transmitted temporal pulse profiles are plotted as the dependence on input fluence for (c–e) different detunings and (h–j) waveguide lengths.

produced by the incident pulse in the area of the input coupler (see the [Supporting Information](#) for details).

The photonic subsystem is coupled to the excitonic subsystem, with the coupling strength characterized by Rabi splitting Ω_R . The coherent excitons are described by the slowly varying envelope amplitude ψ . The losses in the exciton subsystem are defined by the total dissipation rate $\gamma_{\text{ex}} + \gamma_{\text{res}}$, consisting of the coherent exciton decay rate γ_{ex} and the rate of the scattering to the reservoir of the incoherent excitons γ_{res} (incoherent exciton density). The shift of the coherent exciton frequency due to nonlinear effects is accounted for by Δ , which is a function of $|\psi|^2$ and ρ . Describing the dynamics in terms of slowly varying amplitudes, we choose the carrier frequency to be equal to the exciton resonance frequency in the linear regime, so $\Delta(|\psi|^2 = 0, \rho = 0) = 0$.

In the strong exciton-photon coupling regime, excitonic and photonic dispersions anticross, and the resulting exciton-polaritons acquire strong dispersion near the resonance. The dispersion of these hybrid excitations (polaritons) is given by

$$\omega(k) = \frac{v_g k + i(\gamma_{\text{ph}} + \gamma_{\text{ex}} + \gamma_{\text{res}}) \pm \sqrt{(v_g k + i(\gamma_{\text{ph}} - \gamma_{\text{ex}} - \gamma_{\text{res}}))^2 + 4\Omega_R^2}}{2} \quad (2)$$

To reproduce the dynamics observed in the experiments, it is necessary to account for the reservoir of long-living incoherent excitons characterized by density ρ and lifetime γ_ρ . We assume unidirectional scattering from coherent to incoherent excitons with rate γ_{res} . The reservoir may form through scattering into excitonic states within the tail of the inhomogeneously broadened exciton line,^{49,50} where the

density of states is significantly higher than for polaritons. Alternatively, the reservoir can consist of localized excitons, indirect excitons, or other dark excitonic states.^{51–54}

While we assume the photonic component to behave linearly with fluence, for excitons, both the resonance frequency and decay rate are density-dependent. These nonlinear dependencies of the resonant frequency and the losses are accounted for by exciton density-dependent parameters Δ and Γ (see the [Supporting Information](#) for details).

DISCUSSION

We numerically solve the system of equations described above using the split-step method, calculating the photonic field as a function of both the time and position in the waveguide. The model gives good qualitative and quantitative agreements with the experimental data ([Figure 2g–i](#) (lines) and [Figure 3a,b,f,g](#)). The transmittance coefficient of the waveguide, determined by energy integration of the spectra and normalized on fluence for different waveguide lengths and different detunings, is plotted in [Figure 2g](#). We estimate coupling efficiency and account for input and output pulse energies in the experiment (see the [Supporting Information](#) for details). Across all detunings and waveguide lengths, the transmittance behavior observed in the experiment and the model exhibits the same pattern: an initial linear regime (the transmittance does not depend on input fluence; see the [Supporting Information](#)) followed by a nonlinear decrease with rising input fluence; in this nonlinear regime, both transmittance and pulse shape are affected by the input fluence. This phenomenon occurs because nonlinear

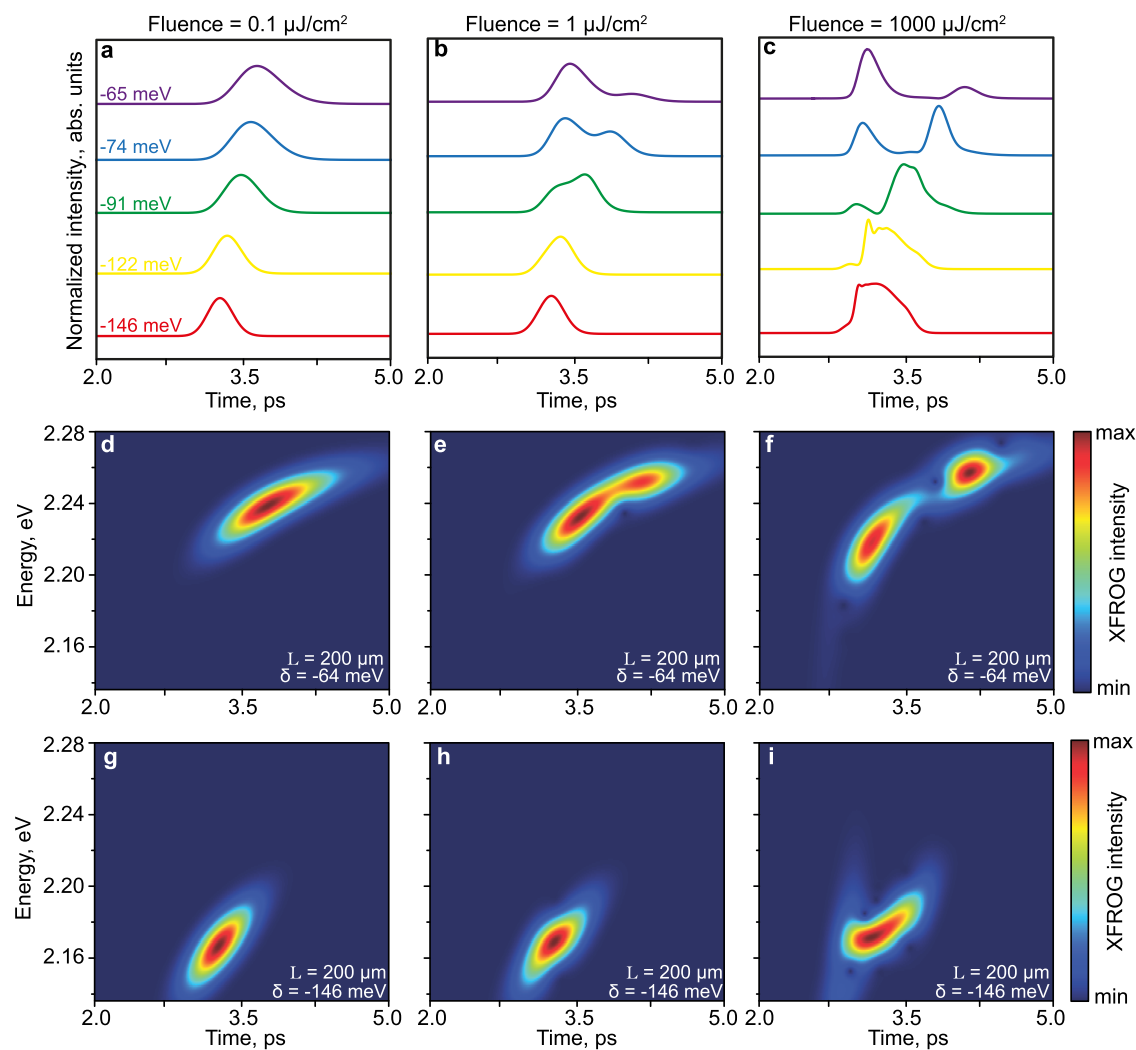


Figure 4. Nonlinear effect of the polaritonic waveguide on pulse propagation. (a–c) Simulated normalized transmitted temporal pulse profiles plotted for different detunings at three fluences. (d–i) Cross-correlation frequency-resolved optical gating (XFROG) for two detunings and different fluence.

losses outweigh the effect of exciton resonance blue shift. In the case of fluence-dependent exciton resonance blue shift, the polariton losses at the same energy decrease, since these losses are primarily determined by the excitonic component. As a result, transmittance increases.²³ However, in MAPbBr₃, nonlinear losses quickly dominate over the blue-shift effect, leading to a net decrease in transmittance. Additionally, the overall transmittance decreases for longer waveguides or detunings, corresponding to higher exciton fractions (Figure 2g). With reduced detuning from the exciton resonance, transmittance declines further due to increased losses, as the exciton fraction—and thus polariton loss—rises. Near the exciton resonance, effective losses γ_{eff} increase, while the group velocity v_g decreases, jointly reducing the waveguide transmittance.

Increasing the input pulse energy blue-shifts the exciton resonance, reducing the difference in absorption rates across frequencies. This decrease in absorption variation lowers the red shift of the output pulse at higher pump powers, leading the central frequency of the output spectrum to shift toward the blue side of the spectrum. Changes in peak position are governed by two parameters related to shifts in the central exciton frequency, α_3 and α_5 , corresponding to 2-particle and

3-particle interactions as discussed in Supporting Information. The parameter α_3 is positive, contributing to an increase in the exciton frequency (a blue shift), while α_5 is negative, leading to a saturation in the exciton frequency shift.²⁵ As the input fluence increases, α_3 initially dominates, followed by a significant contribution from α_5 . Consequently, both the experimental and numerical data reveal an initial blue shift followed by the shift saturation as the input fluence increases (Figure 2h). Once the blue shift reaches saturation, a red shift occurs as incoherent excitons absorb higher frequencies, effectively shifting the pulse toward the red side of the spectrum.

In both theoretical and experimental data, the spectral separation between the two peaks widens with increasing fluence. The high-energy peaks are well captured by the model, displaying an initial blue shift followed by a red shift, consistent with experimental observations (Figure 2h). For the low-energy peaks, the model predicts only red shifts, without the initial blue shift observed experimentally. This discrepancy may arise because the model accounts only for one-dimensional propagation and does not fully accommodate variations in coupling strength at different detunings along with minor mismatches in input energy. Additionally, slight variations in

the input pulse shape, which cannot be directly measured, are expected.

Figure 2i demonstrates the relative change in spectral line width compared to the initial line width at low fluence, as the fluence varies. The spectral peak initially narrows and then broadens across all detunings and waveguide lengths. This behavior of the pulse width is common for the solitonic regime of propagation.¹⁸ Weak linear losses lead to spectral compression by adding a perturbative term to the nonlinear Schrodinger equation (NSE). As the pulse loses energy, its peak power and nonlinear phase shift decrease, necessitating a narrower spectrum to balance nonlinear and dispersion lengths. There is strong agreement between the experiment and the simulation, with discrepancies only appearing at high fluences, where higher-order nonlinearities may need to be incorporated into the model.

Figure 3 shows normalized transmittance spectra plotted in the dependence of input fluence for different detunings and waveguide lengths alongside a comparison with numerical data. The experimental spectra presented in Figure 3a for $\delta = -64$ meV and $L = 200 \mu\text{m}$ and in Figure 3f for $\delta = -74$ meV and $L = 50 \mu\text{m}$ are in good agreement with our calculated result in Figure 3b,g. Both the experimental and theoretical results show two distinct spectral peaks with similar trends in central frequency shifts and line width. In the experiment, the pulse structure appears more symmetric, resembling classical self-phase modulation, while in the model, the shape of the low-energy peak shows a slight variation. This difference may result from minor variations in the input pulse shape.

We propose the presence of two key nonlinear effects in the perovskite waveguide under strong light–matter coupling: interplay between self-phase modulation (SPM) and nonlinear group velocity dispersion (GVD), and self-steepening, both of which play crucial roles in shaping the output pulse dynamics. In contrast to traditional fiber systems,³ the nonlinear processes here are associated with exciton-polariton dispersion and its nonlinear behavior. The first process, balancing of SPM and GVD, leads to soliton formation.^{55,56} This effect symmetrizes the pulse in the time domain, countering the inherent asymmetry caused by dispersion. In a linear regime, output pulses tend to be distorted due to dispersion effects, but the soliton regime restores symmetry by balancing dispersion and nonlinearity.^{18,57} The second process is the so-called self-steepening effect, whose physical origin is the dependence of the group velocity on the local intensity of the field. The self-steepening results in the formation of shock waves.⁵⁸ This phenomenon is well known in fiber optics⁵⁹ and consists of the formation of a sharp leading edge followed by a slowly decaying tail.

One of the main advantages of exciton-polariton systems is the potential to explore different regimes of nonlinear pulse dynamics by tuning the pump frequency. Based on the numerical results that align well with our experimental findings, we propose that varying the pump frequency allows us to transition between shock wave formation and soliton regimes. Hence, we calculate the temporal profiles of the photonic field shown in Figure 3. At higher detuning, the system predominantly exhibits shock-wave behavior, characterized by a sharp leading edge and a decaying tail due to self-steepening (Figure 3e). As the detuning decreases, we observe a transition where two solitons emerge, driven by the balance between self-phase modulation and group velocity dispersion, leading to a symmetric pulse profile (Figure 3c,d).

The wavelength also plays a critical role. In shorter waveguides, shock waves dominate due to limited interaction length (Figure 3h). However, as the waveguide length increases, the system has more space for nonlinear interactions to evolve. This results in the formation of solitons as oscillations behind the shock front deepen and stabilize into solitonic trains (Figure 3i,j). We want to highlight that our system exhibits a strongly nonlinear response, allowing us to observe significant nonlinear effects even in relatively short waveguides with the length of $L = 50 \mu\text{m}$ (as compared with optical fibers), which has the potential to be applied in room-temperature on-chip devices.

The discussed dynamics are clearly visible in the modeled temporal profiles shown in Figure 4a–c, where decreasing detuning transitions the system from shock wave formation to soliton formation. Specifically, under certain pump conditions (Figure 4c), our modeling reveals oscillations trailing the shock front that gradually deepen, eventually forming a pair of solitons. This observation suggests that shock waves and solitons are not isolated phenomena but rather exist on a continuum of behaviors influenced by input parameters such as pump fluence and frequency and by the system parameters, in particular by the nonlinearity dispersion caused by an incoherent excitons reservoir.

In our experiment, only the spectral domain is accessible. In Figure 4d–i, we present the cross-correlation frequency-resolved optical gating (XFROG) data from the model for various input fluences and detunings (see the Supporting Information for details and different waveguide lengths). XFROG enables a comparison of experimentally obtained spectra with theoretical temporal profiles, capturing the evolution of the transmitted pulse in the spectral-temporal domain. For detuning $\delta = -64$ meV and a waveguide length of $L = 200 \mu\text{m}$ (Figure 4d–f), there is a distinct splitting of the transmitted pulse into two separate peaks with increasing fluence from 0.1 to 1000 $\mu\text{J}/\text{cm}^2$, attributed to self-phase modulation. Additionally, the changing slope of this structure indicates variations in the group velocity. For detuning $\delta = -146$ meV and waveguide length $L = 200 \mu\text{m}$ (Figure 4g–i), the changing slope is further associated with nonlinear group velocity dispersion, leading to a steep front formation that may represent a shock wave.

CONCLUSION

We have revealed a strong effect of self-phase modulation and nonlinear group velocity dispersion in the planar submillimeter 2D polaritonic waveguide based on halide MAPbBr₃ perovskite at room temperature. The experiments were carried out by exciting the guided exciton-polaritons using a femtosecond laser resonantly coupled into the waveguide via imprinted grating. Due to polariton–polariton interaction, the pulse transmittance exhibits vivid nonlinearity for fluences above 5 $\mu\text{J}/\text{cm}$. The SPM manifests itself in changes in the spectral pulse shape during pulse propagation through the waveguide, which depends on the incident laser fluence. The theoretical analysis has revealed that SPM induces the temporal splitting of the input pulse into two separate pulses and drives the system into the quasi-soliton and shock-wave regimes. The transition between different nonlinear regimes can be achieved by tuning the pump energy. Our findings are supported by a detailed experimental study containing wavelength- and distance-dependent fs-pulse propagation and the theoretical model that complements experimental data.

Generally, the strong optical nonlinearity from polariton–polariton interactions in perovskite waveguides enables the exploration of diverse nonlinear phenomena such as solitons, shock waves, and SPM in planar polaritonic systems. This pronounced nonlinearity suggests the possibility to control pulse propagation using a control pulse, which will be the subject of further studies. This concept can be easily applied to the future of perovskite on-chip polaritonics, offering superior reproducibility, scalability, and cost-effectiveness compared to traditional waveguiding platforms, which rely on external cavities for similar nonlinear effects in integrated photonic devices.

METHODS

Sample Fabrication. Perovskite waveguides are fabricated utilizing spin coating and nanoimprint techniques. The first step of thin film fabrication is preparing the perovskite solution. The perovskite solution is prepared in a glovebox nitrogen atmosphere using two salts: methylammonium bromide (MABr) and lead(II) bromide (PbBr₂). The mass of salts is calculated based on the molarity of the solution equal to 0.5, $m_{\text{MABr}} = 55.98$ mg and $m_{\text{PbBr}_2} = 183.51$ mg. Salts were dissolved in a 1 mL mixture of dimethylformamide (DMF) and dimethyl sulfoxide (DMSO), in the ratio DMF:DMSO 3:1. Before synthesizing the thin film, 12×12 mm² SiO₂ substrates were cleaned sequentially with soapy water, acetone, and isopropanol. To achieve the higher attribute of surface adhesion, we put substrates in the oxygen plasma cleaning camera for 10 min. The spin coating process is carried out in a glovebox with a dry nitrogen atmosphere because of sensitivity to oxygen concentration. The prepared perovskite solution is deposited on top of the substrate, and after it accelerates for 3 s and rotates at a speed of 3000 rpm for 45 s with the spilling of dry chlorobenzene at 25 s from the beginning of the spin coating. Thus, we obtain a thin film of perovskite MAPbBr₃ with a thickness of roughly 110 nm.

The nanoimprint glass master molds are fabricated by electron beam lithography. First, the fused silica wafers (1×1 cm²) are cleaned by the Hellmanex and DI water solution for 15 min in the sonicator, followed by the acetone and isopropanol in the sonicator. Then, those wafers are cleaned with a standard Piranha solution (H₂SO₄/H₂O₂ = 3:1) in the cleanroom. Next, the Piranha cleaned wafers are dried by N₂ gas flow and placed on a hot plate before depositing the e-beam resist. Using a spinner, an e-beam resist (PMMA 950 A2) is deposited on wafers to get the target thickness of PMMA for the lift-off procedure, followed by a postbaking of 3 min on the hot plate. The fused silica wafer and PMMA are dielectric nonconductors that can accumulate charge during electron beam lithography (EBL) patterning. To avoid the charging problem, a very thin layer (7 nm) of conducting polymer E-Spacer 300Z (SHOWA DENKO) is coated on PMMA using a spinner. Then, the wafers are placed in the EBL (FEI Nova NanoSEM 600) chamber. After patterning with a dose value of 250 $\mu\text{C}/\text{cm}^2$, E-Spacer is removed at first by rinsing in DI water for 1 min. Then, PMMA is developed by the MIBK/IPA solution (1:3) for 1 min, followed by IPA and DI for 20 s, respectively. The EBL patterned wafers are placed in the e-beam evaporator (MIDAS e-beam Evaporator) chamber to deposit a 15 nm thick chromium (Cr). After the pattern was checked with the scanning electron beam microscope (SEM) with the Cr, wafers are rinsed in acetone for the lift-off process. A sonicator is also used to accelerate the lift-off process. Then, those wafers are dried up with N₂ gas flow and placed in the inductively coupled plasma (ICP) (STS Multiplex ICP) chamber to transfer the pattern to a fused silica wafer. A mixer of CHF₃, SF₆, and O₂ (20, 20, and 4 sccm) gas is used to etch down the fused silica where Cr is used as a hard mask. Finally, the unwanted Cr is removed by using chrome etchant, and dry wafers with patterns are stored in a glovebox.

The next stage of fabrication is the optimization of nanoimprint parameters for the fabrication of waveguides based on the perovskite thin film. It is empirically determined that the necessary pressure

exerted for 10 min on the synthesized perovskite sample with dimensions of 12×12 mm² is 40 MPa. After that, the synthesized samples are subjected to thermal influence at a temperature of 90 °C for 10 min. As a result, waveguides with radiation input and output grating elements that repeat the geometry of the master mold are obtained. The fabrication scheme of the waveguides is shown in [Supporting Information](#). The geometry of the fabricated structures is the inverse geometry of the master mold. Thus, waveguides based on a perovskite thin film with a length in the range of 50–200 μm and a period in the range of 260–320 nm with a modulation of 65 nm were fabricated. The couplers and decouplers are characterized using AFM and are shown in [Figure S2](#). It is important to note that master molds can be used multiple times. They were cleaned with DI water and dried before reuse.

Angle-Resolved Spectroscopy. Angle-resolved spectroscopy measurements are performed using a 4f setup featuring a back-focal plane (BFP). This arrangement includes a slit spectrometer connected to an imaging EMCCD camera (Andor Technologies Kymera 328i-B1+ Newton EMCCD DU970P-BVF) and a halogen lamp, which is attached to an optical fiber via a collimation lens for white light illumination. A Mitutoyo Plan Apo Infinity Corrected objective with 10 \times magnification and a numerical aperture of 0.28 is used for excitation and signal collection. Spatial filtering occurs within the intermediate image plane (IP) as it passes through the 4f configuration. Angle-resolved resonant measurements are also conducted using the same setup, employing a femtosecond laser with a tunable wavelength, a repetition rate of 1 kHz, and a pulse width of 200 fs. The laser system includes a mode-locked Ti:sapphire laser operating at 800 nm, which serves as a seed pulse for the regenerative amplifier (Spectra Physics, Spitfire Pro). The wavelength is frequency-doubled to 400 nm using a BBO crystal or combined with an optical parametric amplifier for other pump wavelengths (Light Conversion, OPA). To create a pump spot approximately 50 μm in size, a lens with a 1000 mm focal length is used to focus the laser beam in the BFP. A CCD camera (Thorlabs 1.6 MP Color CMOS Camera DCC1645C) is used in the collection channel, with a 150 mm tube lens positioned after the beam splitter. This setup allows for imaging in both real and Fourier spaces. To resonantly excite the waveguide mode with a femtosecond laser, we select the appropriate wavelength based on the dispersion of the leaky modes ([Figure S4a](#)). The laser spot is positioned on the coupler, and the resonant angle is determined by adjusting the laser's incident angle in the BFP to match the correct wavevector (k_x) corresponding to the dispersion ([Figure 1c](#)), while simultaneously maximizing the output signal from the decoupler in real space.

ASSOCIATED CONTENT

Supporting Information

The Supporting Information is available free of charge at <https://pubs.acs.org/doi/10.1021/acsnano.4c18847>.

Details on the sample fabrication process with AFM characterization, scheme of the optical setup, measured angle-resolved reflectance and transmittance spectra, fitting of polariton modes, coupling efficiency calculations, linear dependence on input fluence, extended theoretical description, input pulse shape, effect of the reservoir on pulse propagation, fitting of transmitted spectra, and cross-correlation frequency-resolved optical gating analysis for different waveguide lengths. ([PDF](#))

AUTHOR INFORMATION

Corresponding Authors

Anton K. Samusev – *Experimentelle Physik 2, Technische Universität Dortmund, 44227 Dortmund, Germany;*

orcid.org/0000-0002-3547-6573;

Email: anton.samusev@gmail.com

Sergey V. Makarov – School of Physics and Engineering, ITMO University, St. Petersburg 197101, Russia; Qingdao Innovation and Development Center, Harbin Engineering University, Qingdao 266000 Shandong, China; orcid.org/0000-0002-9257-6183; Email: s.makarov@metalab.ifmo.ru

Authors

Nikita V. Glebov – School of Physics and Engineering, ITMO University, St. Petersburg 197101, Russia; Institute of Bioengineering, École Polytechnique Fédérale de Lausanne, Lausanne 1015, Switzerland; orcid.org/0000-0002-9026-6106

Mikhail A. Masharin – Institute of Bioengineering, École Polytechnique Fédérale de Lausanne, Lausanne 1015, Switzerland

Alexei Yulin – School of Physics and Engineering, ITMO University, St. Petersburg 197101, Russia

Alexey Mikhin – School of Physics and Engineering, ITMO University, St. Petersburg 197101, Russia; orcid.org/0009-0006-0127-8276

Md Rumon Miah – Department of Electrical and Electronics Engineering, Department of Physics, UNAM – Institute of Materials Science and Nanotechnology and The National Nanotechnology Research Center, Bilkent University, Ankara 06800, Turkey

Hilmi Volkan Demir – Department of Electrical and Electronics Engineering, Department of Physics, UNAM – Institute of Materials Science and Nanotechnology and The National Nanotechnology Research Center, Bilkent University, Ankara 06800, Turkey; Luminous! Center of Excellence for Semiconductor Lighting and Displays, School of Electrical and Electronic Engineering, School of Physical and Mathematical Sciences, and School of Materials Science and Engineering, Nanyang Technological University, Singapore 639798, Singapore; orcid.org/0000-0003-1793-112X

Dmitry N. Krizhanovskii – Department of Physics and Astronomy, University of Sheffield, Sheffield S3 7RH, United Kingdom; orcid.org/0000-0002-6436-7384

Vasily Kravtsov – School of Physics and Engineering, ITMO University, St. Petersburg 197101, Russia; orcid.org/0000-0002-3555-1027

Complete contact information is available at: <https://pubs.acs.org/10.1021/acsnano.4c18847>

Notes

The authors declare no competing financial interest.

ACKNOWLEDGMENTS

This research was supported by Priority 2030 Federal Academic Leadership Program and the National Natural Science Foundation of China (project 62350610272). H.V.D. gratefully acknowledges support from TUBA – Turkish Academy of Sciences. N.V.G. thanks Ivan Sinev for the valuable discussion on the visual representation of results.

REFERENCES

- (1) Chai, Z.; Hu, X.; Wang, F.; Niu, X.; Xie, J.; Gong, Q. Ultrafast all-optical switching. *Adv. Opt. Mater.* **2017**, *5*, No. 1600665.
- (2) Ballarini, D.; De Giorgi, M.; Cancellieri, E.; Houdré, R.; Giacobino, E.; Cingolani, R.; Bramati, A.; Gigli, G.; Sanvitto, D. All-optical polariton transistor. *Nat. Commun.* **2013**, *4*, No. 1778.

- (3) Dudley, J. M.; Genty, G.; Coen, S. Supercontinuum generation in photonic crystal fiber. *Rev. Mod. Phys.* **2006**, *78*, 1135–1184.
- (4) Walker, P. M.; Whittaker, C. E.; Skryabin, D. V.; Cancellieri, E.; Royall, B.; Sich, M.; Farrer, I.; Ritchie, D. A.; Skolnick, M. S.; Krizhanovskii, D. N. Spatiotemporal continuum generation in polariton waveguides. *Light: Sci. Appl.* **2019**, *8*, 6.
- (5) Zhao, C.; Zhang, H.; Qi, X.; Chen, Y.; Wang, Z.; Wen, S.; Tang, D. Ultra-short pulse generation by a topological insulator based saturable absorber. *Appl. Phys. Lett.* **2012**, *101*, No. 211106.
- (6) Kauranen, M.; Zayats, A. V. Nonlinear plasmonics. *Nat. Photonics* **2012**, *6*, 737–748.
- (7) Khitrova, G.; Gibbs, H. M.; Jahnke, F.; Kira, M.; Koch, S. W. Nonlinear optics of normal-mode-coupling semiconductor microcavities. *Rev. Mod. Phys.* **1999**, *71*, 1591–1639.
- (8) Sanvitto, D.; Timofeev, V. *Exciton Polaritons in Microcavities: New Frontiers*; Springer Science & Business Media, 2012; Vol. 172.
- (9) Walker, P. M.; Tinkler, L.; Durska, M.; Whittaker, D.; Luxmoore, I.; Royall, B.; Krizhanovskii, D.; Skolnick, M.; Farrer, I.; Ritchie, D. Exciton polaritons in semiconductor waveguides. *Appl. Phys. Lett.* **2013**, *102*, No. 012109, DOI: [10.1063/1.4773590](https://doi.org/10.1063/1.4773590).
- (10) Deng, H.; Haug, H.; Yamamoto, Y. Exciton-polariton Bose-Einstein condensation. *Rev. Mod. Phys.* **2010**, *82*, 1489.
- (11) Sanvitto, D.; Kéna-Cohen, S. The road towards polaritonic devices. *Nat. Mater.* **2016**, *15*, 1061–1073.
- (12) Tassone, F.; Yamamoto, Y. Exciton-exciton scattering dynamics in a semiconductor microcavity and stimulated scattering into polaritons. *Phys. Rev. B* **1999**, *59*, 10830–10842.
- (13) Masharin, M. A.; Shahnazaryan, V. A.; Benimetskiy, F. A.; Krizhanovskii, D. N.; Shelykh, I. A.; Iorsh, I. V.; Makarov, S. V.; Samusev, A. K. Polaron-enhanced polariton nonlinearity in lead halide perovskites. *Nano Lett.* **2022**, *22*, 9092–9099.
- (14) Suárez-Forero, D.; Riminucci, F.; Ardizzone, V.; Karpowicz, N.; Maggolini, E.; Macorini, G.; Lerario, G.; Todisco, F.; De Giorgi, M.; Dominici, L.; et al. Enhancement of parametric effects in polariton waveguides induced by dipolar interactions. *Phys. Rev. Lett.* **2021**, *126*, No. 137401.
- (15) Emmanuele, R. P. A.; Sich, M.; Kyriienko, O.; Shahnazaryan, V.; Withers, F.; Catanzaro, A.; Walker, P.; Benimetskiy, F.; Skolnick, M.; Tartakovskii, A.; et al. Highly nonlinear trion-polaritons in a monolayer semiconductor. *Nat. Commun.* **2020**, *11*, No. 3589.
- (16) Weisbuch, C.; Nishioka, M.; Ishikawa, A.; Arakawa, Y. Observation of the coupled exciton-photon mode splitting in a semiconductor quantum microcavity. *Phys. Rev. Lett.* **1992**, *69*, 3314.
- (17) Deng, H.; Weihs, G.; Santori, C.; Bloch, J.; Yamamoto, Y. Condensation of semiconductor microcavity exciton polaritons. *Science* **2002**, *298*, 199–202.
- (18) Walker, P. M.; Tinkler, L.; Skryabin, D.; Yulin, A.; Royall, B.; Farrer, I.; Ritchie, D.; Skolnick, M.; Krizhanovskii, D. Ultra-low-power hybrid light-matter solitons. *Nat. Commun.* **2015**, *6*, No. 8317.
- (19) Kasprzak, J.; Richard, M.; Kundermann, S.; Baas, A.; Jeambrun, P.; Keeling, J. M. J.; Marchetti, F.; Szymańska, M.; André, R.; Staehli, J.; et al. Bose-Einstein condensation of exciton polaritons. *Nature* **2006**, *443*, 409–414.
- (20) van Vugt, L. K.; Rühle, S.; Ravindran, P.; Gerritsen, H. C.; Kuipers, F.; Vanmaekelbergh, D. Exciton polaritons confined in a ZnO nanowire cavity. *Phys. Rev. Lett.* **2006**, *97*, No. 147401.
- (21) Semond, F.; Sellers, I.; Natali, F.; Byrne, D.; Leroux, M.; Massies, J.; Ollier, N.; Leymarie, J.; Disseix, P.; Vasson, A. Strong light-matter coupling at room temperature in simple geometry GaN microcavities grown on silicon. *Appl. Phys. Lett.* **2005**, *87*, No. 021102.
- (22) Stepanov, P.; Vashisht, A.; Klaas, M.; Lundt, N.; Tongay, S.; Blei, M.; Höfling, S.; Volz, T.; Minguzzi, A.; Renard, J.; et al. Exciton-exciton interaction beyond the hydrogenic picture in a MoSe₂ monolayer in the strong light-matter coupling regime. *Phys. Rev. Lett.* **2021**, *126*, No. 167401.
- (23) Benimetskiy, F. A.; Yulin, A.; Mikhin, A.; Kravtsov, V.; Iorsh, I.; Skolnick, M.; Shelykh, I.; Krizhanovskii, D.; Samusev, A. Nonlinear self-action of ultrashort guided exciton-polariton pulses in dielectric slab coupled to 2D semiconductor. *2D Mater.* **2023**, *10*, No. 045016.

- (24) Di Paola, D. M.; Walker, P. M.; Emmanuele, R.; Yulin, A. V.; Ciers, J.; Zaidi, Z.; Carlin, J.-F.; Grandjean, N.; Shelykh, I.; Skolnick, M. S.; et al. Ultrafast-nonlinear ultraviolet pulse modulation in an AlInGaN polariton waveguide operating up to room temperature. *Nat. Commun.* **2021**, *12*, No. 3504.
- (25) Masharin, M. A.; Shahnazaryan, V. A.; Iorsh, I. V.; Makarov, S. V.; Samusev, A. K.; Shelykh, I. A. Room-temperature polaron-mediated polariton nonlinearity in MAPbBr₃ perovskites. *ACS Photonics* **2023**, *10*, 691–698.
- (26) Tonkaev, P.; Koshelev, K.; Masharin, M. A.; Makarov, S. V.; Kruk, S. S.; Kivshar, Y. Observation of Enhanced Generation of a Fifth Harmonic from Halide Perovskite Nonlocal Metasurfaces. *ACS Photonics* **2023**, *10*, 1367–1375.
- (27) Makarov, S.; Furasova, A.; Tiguntseva, E.; Hemmetter, A.; Berestennikov, A.; Pushkarev, A.; Zakhidov, A.; Kivshar, Y. Halide-perovskite resonant nanophotonics. *Adv. Opt. Mater.* **2019**, *7*, No. 1800784.
- (28) Xiong, Z.; Wu, H.; Cai, Y.; Zhai, X.; Liu, T.; Li, B.; Song, T.; Guo, L.; Liu, Z.; Dong, Y.; et al. Selective Excitation of Exciton-Polariton Condensate Modes in an Annular Perovskite Microcavity. *Nano Lett.* **2024**, *24*, 4959–4964.
- (29) Zhai, X.; Ma, X.; Gao, Y.; Xing, C.; Gao, M.; Dai, H.; Wang, X.; Pan, A.; Schumacher, S.; Gao, T. Electrically Controlling Vortices in a Neutral Exciton-Polariton Condensate at Room Temperature. *Phys. Rev. Lett.* **2023**, *131*, No. 136901.
- (30) Su, R.; Ghosh, S.; Liew, T. C.; Xiong, Q. Optical switching of topological phase in a perovskite polariton lattice. *Sci. Adv.* **2021**, *7*, No. eabf8049.
- (31) Kędziora, M.; Opala, A.; Mastria, R.; De Marco, L.; Król, M.; Łempicka-Mirek, K.; Tyszcza, K.; Ekielski, M.; Guzewicz, M.; Bogdanowicz, K.; et al. Pre-designed perovskite crystal waveguides for room-temperature exciton-polariton condensation and edge lasing. *Nat. Mater.* **2024**, *23*, 1515–1522.
- (32) Jeon, N. J.; Noh, J. H.; Kim, Y. C.; Yang, W. S.; Ryu, S.; Seok, S. I. Solvent engineering for high-performance inorganic-organic hybrid perovskite solar cells. *Nat. Mater.* **2014**, *13*, 897–903.
- (33) McCleese, C. L.; Brennan, M. C.; Episcopo, N.; Sun, L.; Hong, N.; Ramana, C. V.; Grusenmeyer, T. A.; Stevenson, P. R. Optical Dispersion Data Analysis of Single-Crystal CH₃NH₃PbBr₃ for Optimized Perovskite Solar Cell Active Layer Absorptance. *Adv. Photonics Res.* **2024**, *5*, No. 2400019.
- (34) Snyder, A. W.; Love, J. D. *Optical Waveguide Theory*, 1st ed.; Springer: New York, 1983; pp 240–248.
- (35) Cheng, L.; Mao, S.; Li, Z.; Han, Y.; Fu, H. Grating couplers on silicon photonics: Design principles, emerging trends and practical issues. *Micromachines* **2020**, *11*, 666.
- (36) Makarov, S. V.; Milichko, V.; Ushakova, E. V.; Omelyanovich, M.; Cerdan Pasaran, A.; Haroldson, R.; Balachandran, B.; Wang, H.; Hu, W.; Kivshar, Y. S.; Zakhidov, A. A. Multifold emission enhancement in nanoimprinted hybrid perovskite metasurfaces. *ACS Photonics* **2017**, *4*, 728–735.
- (37) Masharin, M. A.; Samusev, A.; Bogdanov, A.; Iorsh, I.; Demir, H. V.; Makarov, S. Room-Temperature Exceptional-Point-Driven Polariton Lasing from Perovskite Metasurface. *Adv. Funct. Mater.* **2023**, *33*, No. 2215007.
- (38) Glebov, N.; Masharin, M.; Borodin, B.; Alekseev, P.; Benimetskiy, F.; Makarov, S.; Samusev, A. Mechanical scanning probe lithography of perovskites for fabrication of high-Q planar polaritonic cavities. *Appl. Phys. Lett.* **2023**, *122*, No. 141103.
- (39) Zhizhchenko, A. Y.; Cherepakhin, A.; Masharin, M.; Pushkarev, A.; Kulinich, S.; Porfirev, A.; Kuchmizhak, A.; Makarov, S. Direct imprinting of laser field on halide perovskite single crystal for advanced photonic applications. *Laser Photonics Rev.* **2021**, *15*, No. 2100094.
- (40) Hopfield, J. J. Theory of the contribution of excitons to the complex dielectric constant of crystals. *Phys. Rev.* **1958**, *112*, 1555.
- (41) Schneider, C.; Glazov, M. M.; Korn, T.; Höfling, S.; Urbaszek, B. Two-dimensional semiconductors in the regime of strong light-matter coupling. *Nat. Commun.* **2018**, *9*, No. 2695.
- (42) Kondratyev, V. I.; Permyakov, D. V.; Ivanova, T. V.; Iorsh, I. V.; Krizhanovskii, D. N.; Skolnick, M. S.; Kravtsov, V.; Samusev, A. K. Probing and Control of Guided Exciton-Polaritons in a 2D Semiconductor-Integrated Slab Waveguide. *Nano Lett.* **2023**, *23*, 7876–7882.
- (43) Su, R.; Diederichs, C.; Wang, J.; Liew, T. C.; Zhao, J.; Liu, S.; Xu, W.; Chen, Z.; Xiong, Q. Room-temperature polariton lasing in all-inorganic perovskite nanoplatelets. *Nano Lett.* **2017**, *17*, 3982–3988.
- (44) Fieramosca, A.; Polimeno, L.; Ardizzone, V.; De Marco, L.; Pugliese, M.; Maiorano, V.; De Giorgi, M.; Dominici, L.; Gigli, G.; Gerace, D.; et al. Two-dimensional hybrid perovskites sustaining strong polariton interactions at room temperature. *Sci. Adv.* **2019**, *5*, No. eaav9967.
- (45) Wu, J.; Ghosh, S.; Su, R.; Fieramosca, A.; Liew, T. C.; Xiong, Q. Nonlinear parametric scattering of exciton polaritons in perovskite microcavities. *Nano Lett.* **2021**, *21*, 3120–3126.
- (46) Masharin, M. A.; Oskolkova, T.; Isik, F.; Volkan Demir, H.; Samusev, A. K.; Makarov, S. V. Giant Ultrafast All-Optical Modulation Based on Exceptional Points in Exciton-Polariton Perovskite Metasurfaces. *ACS Nano* **2024**, *18*, 3447–3455.
- (47) Wouters, M.; Carusotto, I. Excitations in a nonequilibrium Bose–Einstein condensate of exciton polaritons. *Phys. Rev. Lett.* **2007**, *99*, No. 140402.
- (48) Skryabin, D. V.; Kartashov, Y.; Egorov, O.; Sich, M.; Chana, J.; Tapia Rodriguez, L.; Walker, P.; Clarke, E.; Royall, B.; Skolnick, M.; Krizhanovskii, D. N. Backward Cherenkov radiation emitted by polariton solitons in a microcavity wire. *Nat. Commun.* **2017**, *8*, No. 1554.
- (49) Whittaker, D. M. What determines inhomogeneous linewidths in semiconductor microcavities? *Phys. Rev. Lett.* **1998**, *80*, 4791.
- (50) Vinattieri, A.; Shah, J.; Damen, T.; Kim, D.; Pfeiffer, L. N.; Maiale, M. Z.; Sham, L. J. Exciton dynamics in GaAs quantum wells under resonant excitation. *Phys. Rev. B* **1994**, *50*, No. 10868.
- (51) Krizhanovskii, D.; Dasbach, G.; Dremine, A.; Kulakovskii, V.; Gippius, N.; Bayer, M.; Forchel, A. Impact of exciton localization on the optical non-linearities of cavity polaritons. *Solid State Commun.* **2001**, *119*, 435–439.
- (52) Sarkar, D.; Gavrilo, S.; Sich, M.; Quilter, J.; Bradley, R.; Gippius, N.; Guda, K.; Kulakovskii, V.; Skolnick, M.; Krizhanovskii, D. Polarization bistability and resultant spin rings in semiconductor microcavities. *Phys. Rev. Lett.* **2010**, *105*, No. 216402.
- (53) Ménard, J.-M.; Pöllmann, C.; Porer, M.; Leierseder, U.; Galopin, E.; Lemaître, A.; Amo, A.; Bloch, J.; Huber, R. Revealing the dark side of a bright exciton-polariton condensate. *Nat. Commun.* **2014**, *5*, No. 4648.
- (54) Tollerud, J. O.; Cundiff, S. T.; Davis, J. A. Revealing and characterizing dark excitons through coherent multidimensional spectroscopy. *Phys. Rev. Lett.* **2016**, *117*, No. 097401.
- (55) Agrawal, G. P. *Nonlinear Fiber Optics*, 6th ed.; Agrawal, G. P., Ed.; Academic Press, 2019; pp 127–187.
- (56) Kivshar, Y. S.; Agrawal, G. P. *Optical Solitons: From Fibers to Photonic Crystals*; Academic Press, 2003; pp 63–66.
- (57) Yulin, A. V.; Zezyulin, D. Bright and dark solitons in the systems with strong light-matter coupling: Exact solutions and numerical simulations. *Phys. Rev. E* **2022**, *106*, No. 044202.
- (58) DeMartini, F.; Townes, C.; Gustafson, T.; Kelley, P. Self-steepening of light pulses. *Phys. Rev.* **1967**, *164*, 312.
- (59) Agrawal, G. P. *Nonlinear Fiber Optics*, 6th ed.; Agrawal, G. P., Ed.; Academic Press, 2019; pp 85–125.